Ceramics International 44 (2018) 4237–4247

Contents lists available at ScienceDirect

Ceramics International

journal homepage: www.elsevier.com/locate/ceramint

Solution combustion synthesis of nanostructured iron oxides with controllable morphology, composition and electrochemical performance

Xuanli Wang[a], Mingli Qin[a,*], Fei Fang[a], Baorui Jia[a], Haoyang Wu[a], Xuanhui Qu[a], Alex A. Volinsky[b]

[a] Institute for Advanced Materials and Technology, University of Science and Technology Beijing, Beijing 100083, China
[b] Department of Mechanical Engineering, University of South Florida, Tampa, FL 33620, USA

ARTICLE INFO

Keywords:
Solution combustion synthesis
Nanostructured iron oxides
Controllable morphology and composition
Electrochemical properties

ABSTRACT

Nanostructured iron oxides have emerged as promising materials for electrochemical energy storage and conversion devices due to their high theoretical capacity, eco-friendliness and earth abundance. Particularly, the morphology- and composition-controllable synthesis of nanostructured iron oxides is extremely important to optimize their electrochemical performance. However, the development of facile and effective synthetic method is still a great challenge. In this paper, we demonstrated a one-pot solution combustion synthesis (SCS) approach for the time- and energy-effective preparation of nanostructured iron oxides with controllable morphology and composition just by tuning the molar ratio (φ) of fuel (glycine) to oxidizer (ferric nitrate). Innovatively, the effects of φ value on the control of combustion reaction mechanism, morphology and composition of SCS products, and the electrochemical properties in relation to the morphology and composition have been systematically investigated. The results revealed that with the increase of φ value, the reaction mechanism varied from pyrolysis to combustion and the combustion phenomenon changed from volumetric mode to self-propagating mode. Correspondingly, the morphology of products evolved from uniform nanoneedles to porous nanosheets, and finally into aggregated nanoparticles. Meanwhile, the phase composition of these products changed from amorphous α-Fe_2O_3 to crystalline α-Fe_2O_3, and eventually into α-Fe_2O_3/Fe_3O_4 composites. When evaluated as lithium ion battery anode, the as-prepared α-Fe_2O_3/Fe_3O_4 porous nanosheets (φ = 1.0 product) exhibited the best electrochemical properties (a high reversible capacity of ~ 1200 mA h g^{-1} and an excellent rate capability) among all the SCS products, which may be attributed to its mesoporous structure (supply favorable accessibility for electrons), nanosheet morphology (shorten the transport length of Li^+) and appropriate proportion of Fe_3O_4 phase (enhance the electronic conductivity). Consequently, the facile SCS method demonstrated here might provide a new methodology for the morphology and composition-controllable synthesis of nanomaterials, for which a number of prospective applications in electrochemical fields can be envisioned.

1. Introduction

Iron oxides, such as hematite (α-Fe_2O_3) and magnetite (Fe_3O_4), have received steadily growing attention during the past few decades owing to their earth abundance, low toxicity and peculiar physicochemical properties [1–4]. As compared to the corresponding bulk counterparts, nanostructured iron oxides exhibit enhanced properties, such as good biocompatibility, superior magnetic properties, excellent gas and light sensing properties, which make them attractive for various applications including biomedicine, magnetic recording media, gas sensors and photocatalysts [5–8]. Besides, in recent years, with the rapid development of electrochemical energy storage and conversion devices, nanostructured iron oxides have also attracted considerable interest in the electrochemical area due to their low cost, environmental benignity, high theoretical capacity and good chemical stability [9–12]. In spite of these distinct advantages, the electrochemical performance of nanostructured iron oxides is still strongly dependent on their morphology and composition, which are generally believed to have significant influences on the diffusion kinetics of ions, transport rate of electrons and structural stability of electrodes in energy conversion and storage systems [13–16]. Therefore, the morphology- and composition-controllable preparation of nanostructured iron oxides is of great importance to explore their optimal electrochemical performance.

As is well known, the wet chemical methods, including hydrothermal, micro-emulsion, co-precipitation and sol-gel method, can easily prepare uniform nanomaterials with controllable morphology and

* Corresponding author.
E-mail address: qinml@mater.ustb.edu.cn (M. Qin).

https://doi.org/10.1016/j.ceramint.2017.12.004
Received 29 August 2017; Received in revised form 7 November 2017; Accepted 1 December 2017
Available online 05 December 2017

Table 1
Reaction systems of different molar ratios (φ) of glycine to ferric nitrate.

φ	Glycine (mol)	Ferric nitrate (mol)	Reaction condition
0	0	0.025	fuel-free
0.5	0.0208	0.025	fuel-lean
1.0	0.0417	0.025	stoichiometric
1.5	0.0625	0.025	fuel-rich

composition just by tuning the reaction conditions due to their unique advantage, that is, they own the ability to fabricate nanomaterials through molecular precursors in aqueous solution, permitting rigorous control of the entire process and allowing the tractable synthesis of "tailor-made" nanomaterials [17–20]. However, these synthetic approaches generally confront the disadvantages of complex apparatus, long duration, elaborate procedure or environmental pollution, which would limit their massive production and practical applications to some extent. Therefore, it is imperative to explore time- and energy-saving method for the simple and scalable preparation of nanostructured iron oxides with controllable morphology and composition in an environmental-benign manner.

During the past few decades, solution combustion synthesis (SCS) has emerged as an extensive employed wet chemical method to fabricate diverse nanomaterials, especially for nano-oxides and composites, due to its obvious advantages of nonpollution, simplicity, scalability, time- and energy-efficiency [21,22]. To be specific, SCS is substantially an exothermic redox reaction between a soluble oxidizer (e.g. metal nitrates) and an organic fuel (e.g. urea, glycine, citric acid, etc.) dissolved in a homogenous aqueous solution (molecular precursors) within a short duration (on the order of seconds) without any additional energy input (in a self-sustained manner) [23,24]. Apparently, the raw materials are non-toxic, low-cost and available, meanwhile, the experimental apparatus and preparation procedures are simple and straightforward. Once the redox reaction occurs, the high self-generated energy derived from combustion could convert metals into the corresponding oxides directly in a few seconds without the requirement of external energy. The short processing duration and energy saving feature make SCS method suitable for the massive production in practical applications [25–27]. Hence, in the present work, we synthesized nanostructured iron oxides with controllable morphology and composition via SCS method just by tuning the molar ratio (φ) of fuel (glycine) to oxidizer (ferric nitrate). The effects of φ value on the control of combustion reaction mechanism, morphology and composition of SCS products, and the electrochemical properties in relation to the morphology and composition have been systematically investigated.

2. Experimental section

2.1. Synthesis

The nanostructured iron oxides were prepared via SCS method by using ferric nitrate [Fe $(NO_3)_3$] as the oxidizer and glycine ($C_2H_5NO_2$) as the fuel. The stoichiometric equilibrium combustion reaction could be represented as follow:

$$Fe(NO_3)_3 + \frac{5}{3}C_2H_5NO_2 = \frac{1}{2}Fe_2O_3 + \frac{10}{3}CO_2 + \frac{25}{6}H_2O + \frac{7}{3}N_2 \quad (1)$$

Among the various tunable parameters in SCS process, the amount of fuel has been verified to play a crucial role in altering the morphology, composition and properties of final products [28]. Thus, in this work, the molar ratio of glycine (variate) to ferric nitrate (constant), denoted as $\varphi = \frac{3}{5} \times n_{Gly}/n_{Fe}$, was taken to be a key tunable parameter, which varied from 0 (fuel-free condition) to 1.5 (fuel-rich condition), as specified in Table 1.

In a typical SCS procedure, Fe $(NO_3)_3$ and $C_2H_5NO_2$ were first mixed under appropriate molar ratio and then dissolved in 50 mL deionized water to get a homogeneous solution. The obtained solution was poured into 500 mL beaker and put on a pre-heated electric furnace (300 °C). As heating continued, the solution boiled with the evolution of a large

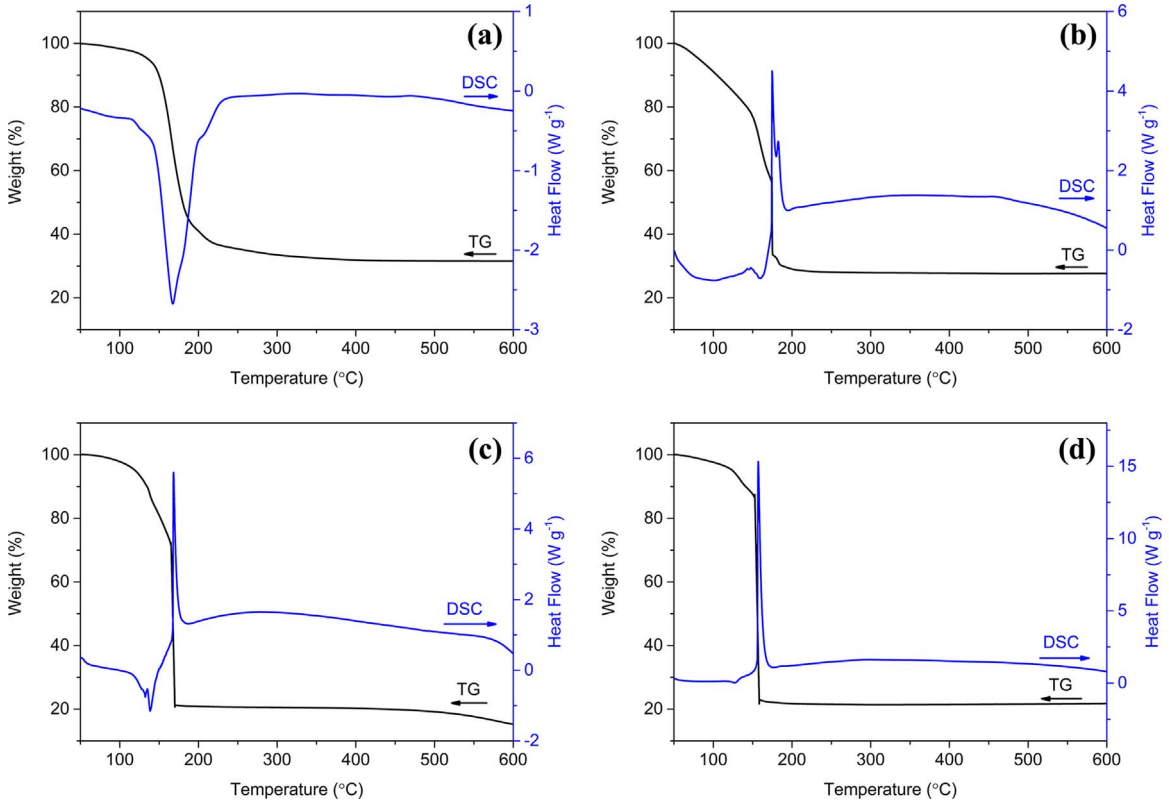

Fig. 1. TG-DSC curves of gel originated from different φ reaction systems: (a) φ = 0; (b) φ = 0.5; (c) φ = 1.0; (d) φ = 1.5.

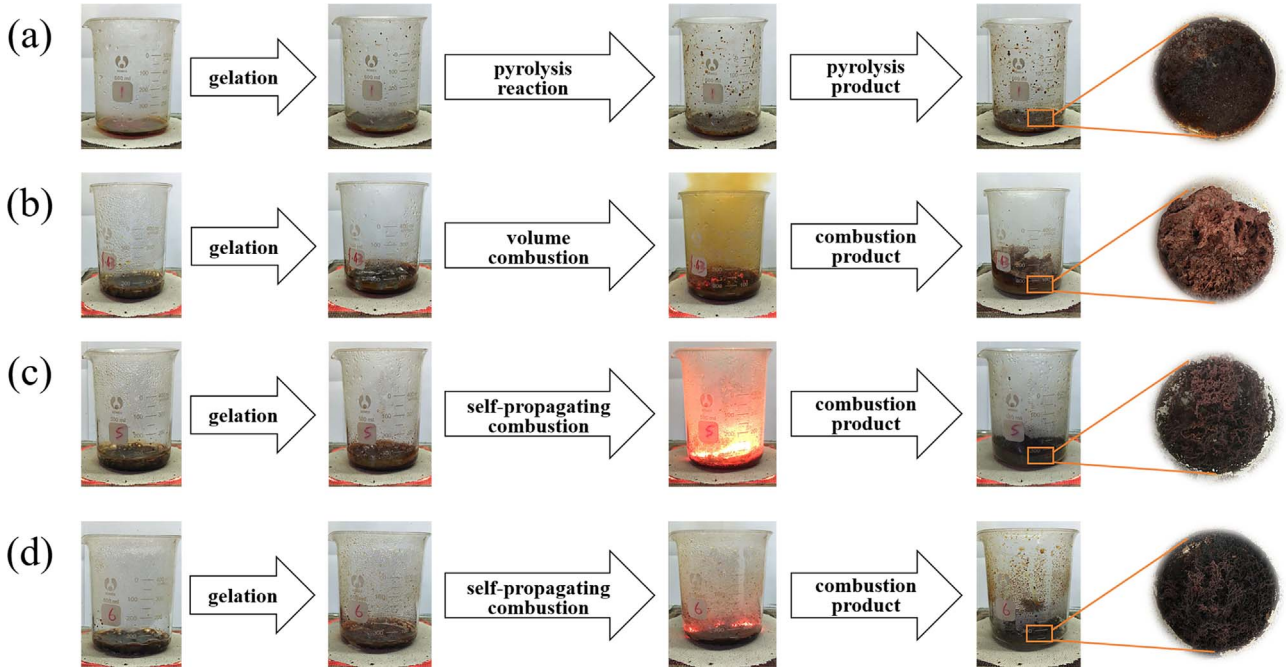

Fig. 2. Reaction process and macro morphology of SCS products obtained from different φ reaction systems: (a) φ = 0; (b) φ = 0.5; (c) φ = 1.0; (d) φ = 1.5.

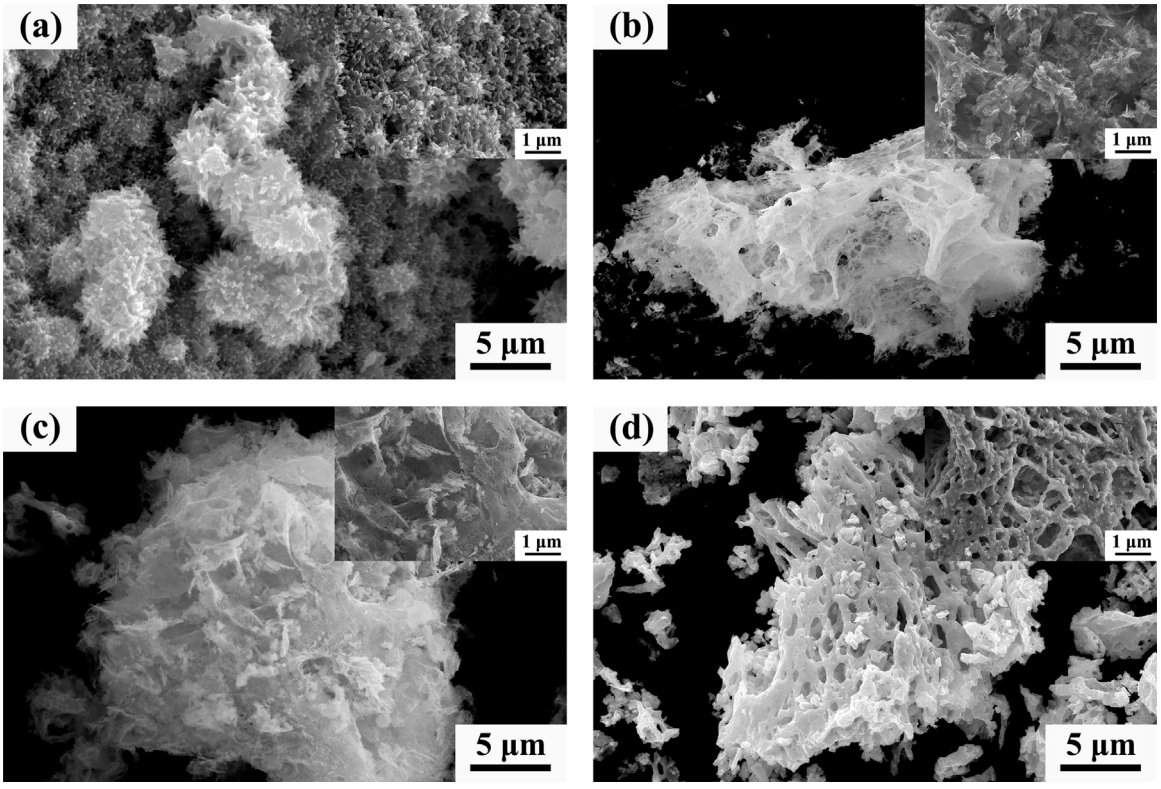

Fig. 3. FE-SEM images of SCS products with different φ (the upper-right inset shows the corresponding high magnification image): (a) φ = 0; (b) φ = 0.5; (c) φ = 1.0; (d) φ = 1.5.

volume of white fume and evolved into a viscous gel. A few minutes later, the viscous gel swelled and a violent combustion reaction suddenly occurred, coupled with the release of voluminous gases. Once the combustion finished, a fluffy material was obtained, that can be easily crumbled into fine powders.

2.2. Characterization

The thermal analysis of gel was performed on a METTLER thermal analyzer (TG-DSC, SF/1382) at a constant heating rate of 10 °C min^{-1} from 50 °C to 600 °C in air. The morphology and microstructural details of SCS products were observed by field emission scanning electron microscopy (FE-SEM, Quanta FEG-450) and further characterized by using transmission electron microscopy (TEM, Tecnai G2 F20). Their

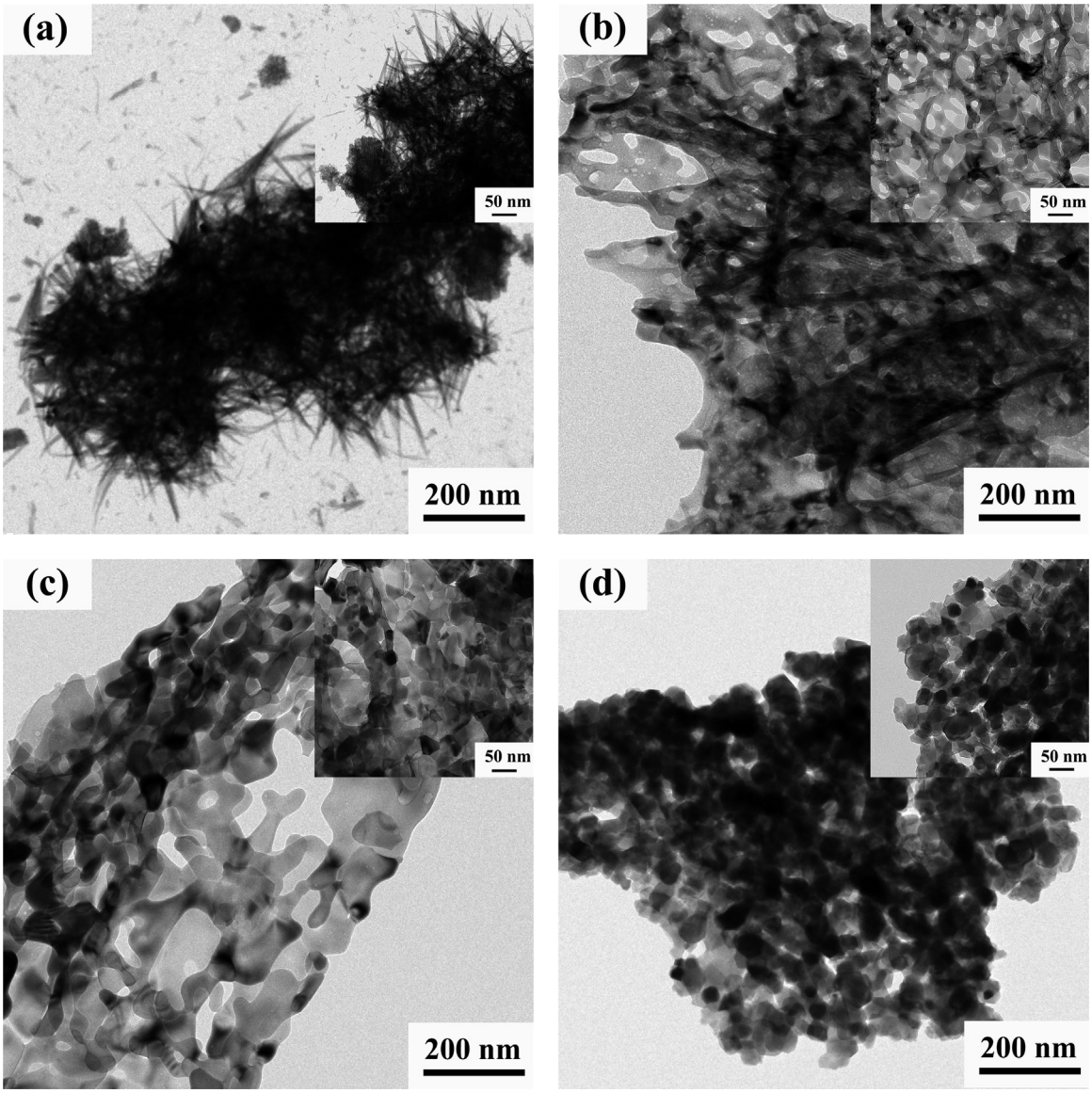

Fig. 4. TEM images of SCS products with different φ (the upper-right inset shows the corresponding high magnification image): (a) φ = 0; (b) φ = 0.5; (c) φ = 1.0; (d) φ = 1.5.

porous structure and specific surface area were determined by a Brunauer-Emmett-Teller (BET) method based on N_2 adsorption-desorption measurements conducted by an automated surface area & pore size analyzer (QUADRASORB SI-MP, Quantachrome Instruments, BoyntonBeach, FL). The phase analysis of SCS products was performed on an X-ray diffractometer (XRD, Ultima IV) and their chemical compositions were analyzed by using an X-ray photoelectron spectroscopy (XPS, Thermo EscaLab 250Xi).

2.3. Electrochemical measurements

To evaluate the electrochemical performance of SCS products, the CR-2032 coin cells were assembled in a high-purity Ar-filled glovebox by using lithium foil, polyethene and 1 M $LiPF_6$ in EC/DMC (1:1, v/v) as the counter electrode, separator membrane and electrolyte, respectively. The working electrode was prepared by compressing the mixture of active material (SCS products), acetylene black and polyvinylidene fluoride, at weight ratios of 60:20:20, onto a copper foil of 14 mm in diameter. The assembled cells were galvanostatic discharged and charged at various current densities within the potential range of 0.01–3.0 V (vs. Li^+/Li) by using a LAND CT2001A battery testing system. Cyclic voltammetry (CV) measurement was conducted at a scan rate of 0.5 mV s^{-1} in the 0.01–3.0 V (vs. Li^+/Li) potential range on an electrochemistry workstation (CHI618D).

3. Results and discussion

To shed light on the reaction mechanism in SCS process, thermogravimetry coupled with differential scanning calorimetry (TG-DSC) was conducted in air from 50 °C to 600 °C. The simultaneous TG-DSC curves of gel originated from different φ reaction systems are depicted in Fig. 1. It is obvious that, up to 200 °C, the φ = 0 reaction system undergoes a large weight loss of ~ 70% and a nearly V-shaped endothermic peak is observed on DSC curve, as shown in Fig. 1(a). This phenomenon can be attributed to the thermal decomposition of ferric nitrate in fuel-free condition. With the addition of fuel, all the φ > 0 reaction systems display a drastic exothermic peak on DSC curve in the range of 150–200 °C accompanied by an abrupt weight loss on TG curve, which are related to the thermally induced redox reaction between ferric nitrate and glycine, as depicted in Eq. (1). Moreover, with the increase of φ value, it can be clearly observed in Fig. 1(b)–(d) that the exothermic peak becomes sharper and the weight loss increases

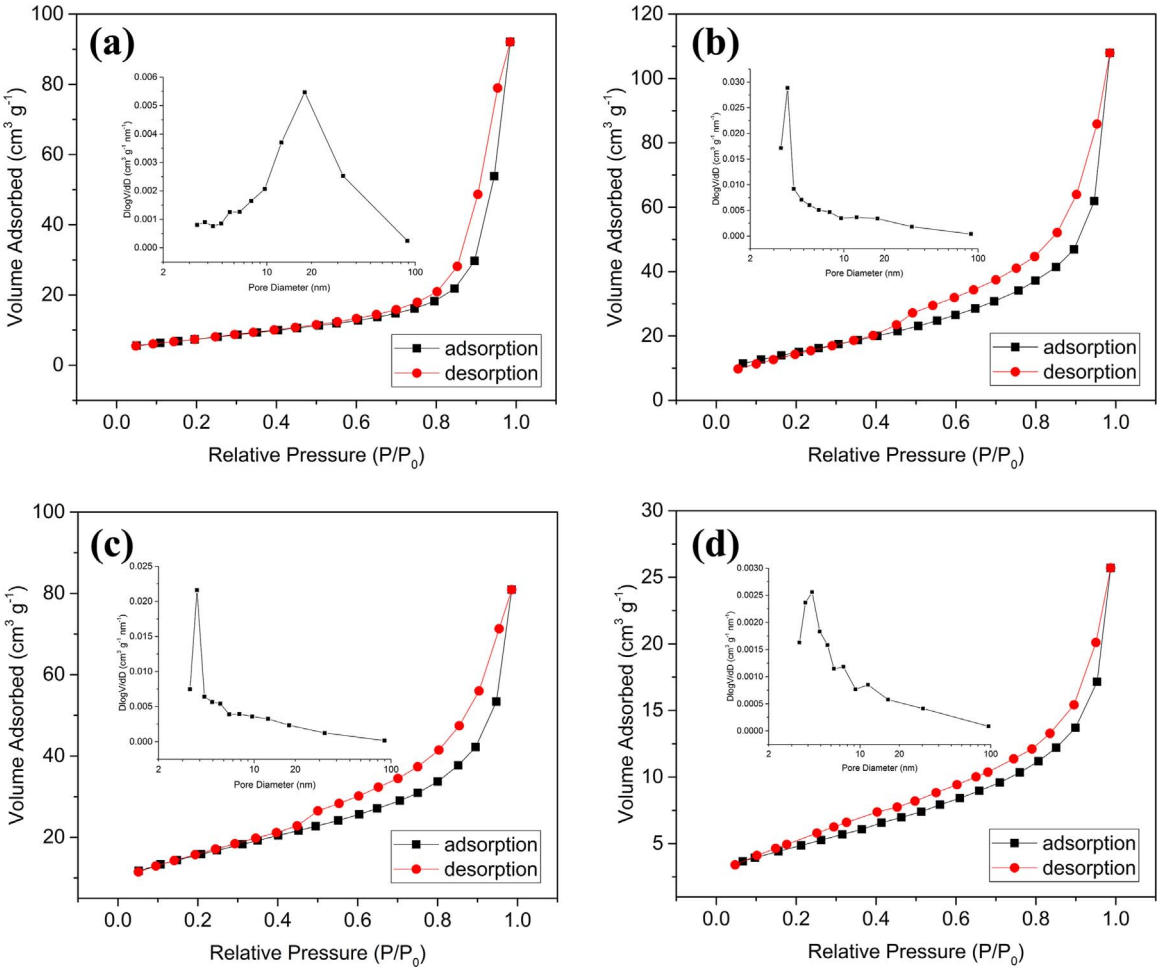

Fig. 5. N_2 adsorption-desorption isotherms and corresponding BJH pore size distribution curves (upper-left inset) of SCS products with different φ: (a) φ = 0; (b) φ = 0.5; (c) φ = 1.0; (d) φ = 1.5.

dramatically (from ~ 30% to ~ 70%), illustrating that the exothermic reaction becomes more intense and thorough as the fuel increasing, thus leading to an instant and significant weight loss of raw materials. Finally, when the temperature exceeds 200 °C, the weight of all the reaction systems keeps almost constant, as shown in Fig. 1(a)–(d), which indicates the end of both endothermic and exothermic reactions.

Fig. 2 shows the visual reaction process and macro morphology of SCS products obtained from different φ reaction systems. In Fig. 2(a), it can be clearly seen that the aqueous solution in φ = 0 reaction system evaporates gradually to form a gel-like substance, accompanied by the continuous splash of hydrothermal liquid. Then, the gel-like substance undergoes a pyrolysis reaction which lasts for a few minutes, leading to the formation of charred dark red powders. It is noteworthy that the entire process requires sustained heating and relatively long duration, indicating that the pyrolysis reaction is a slow and moderate endothermic reaction which is consistent with the TG-DSC analysis in Fig. 1(a). In contrast to this, all the φ > 0 reaction processes involve a transition from aqueous solution to viscous gel and then occur a combustion reaction accompanied by the release of voluminous gases, as shown in Fig. 2(b)–(d). Once the gel is ignited, the high self-generated energy could sustain the whole combustion reaction (in a few seconds) without the requirement of additional heating, suggesting that the combustion reaction is an intense and instant exothermic reaction which is in good agreement with the above TG-DSC analysis. Furthermore, when comparing the combustion reaction phenomena of φ > 0 reaction systems, it can be easily found that the combustion mode varies from volume combustion to self-propagating combustion with the increase of φ value. As shown in Fig. 2(b), φ = 0.5 reaction system exhibits a volume combustion mode, i.e. the reaction breaks out among the gel, accompanied by open flame and dense smoke, and then finishes quickly within ten seconds or so, producing some fluffy spongy red powders. Considering the red color of the obtained powders, it can be inferred that the phase of φ = 0.5 product may be α-Fe_2O_3. With the increase of φ value, it can be clearly observed in Fig. 2(c) that φ = 1.0 reaction system displays a combination mode of volume combustion and self-propagating combustion. Although the reaction is accompanied by a violent flame, it is not an instantaneous burst but tends to spread until swallowing the entire volume of gel, forming some loose dendritic red and black powders, indicating the existence of both α-Fe_2O_3 and Fe_3O_4 phases. When the φ value continues to increase, the φ = 1.5 reaction system in Fig. 2(d) totally presents a self-propagating combustion mode, i.e. the flame starts at a certain point of gel and then spreads to the whole mass, accompanied by the release of voluminous gases. It is worth noting that the self-propagating combustion reaction will last for twenty seconds or so, which is longer than the volume combustion reaction. Because the excessive fuel in φ = 1.5 reaction system requires more oxygen to maintain the combustion reaction, therefore, the self-propagating combustion mode exhibits a slower heating rate and longer reaction time than volume combustion mode. As expected, the combustion product of φ = 1.5 reaction system is also loose dendritic red and black powders but the proportion of red part is reduced when compared with φ = 1.0 product, indicating the decrease of α-Fe_2O_3 phase in φ = 1.5 product.

To acquire more information about morphology of SCS products

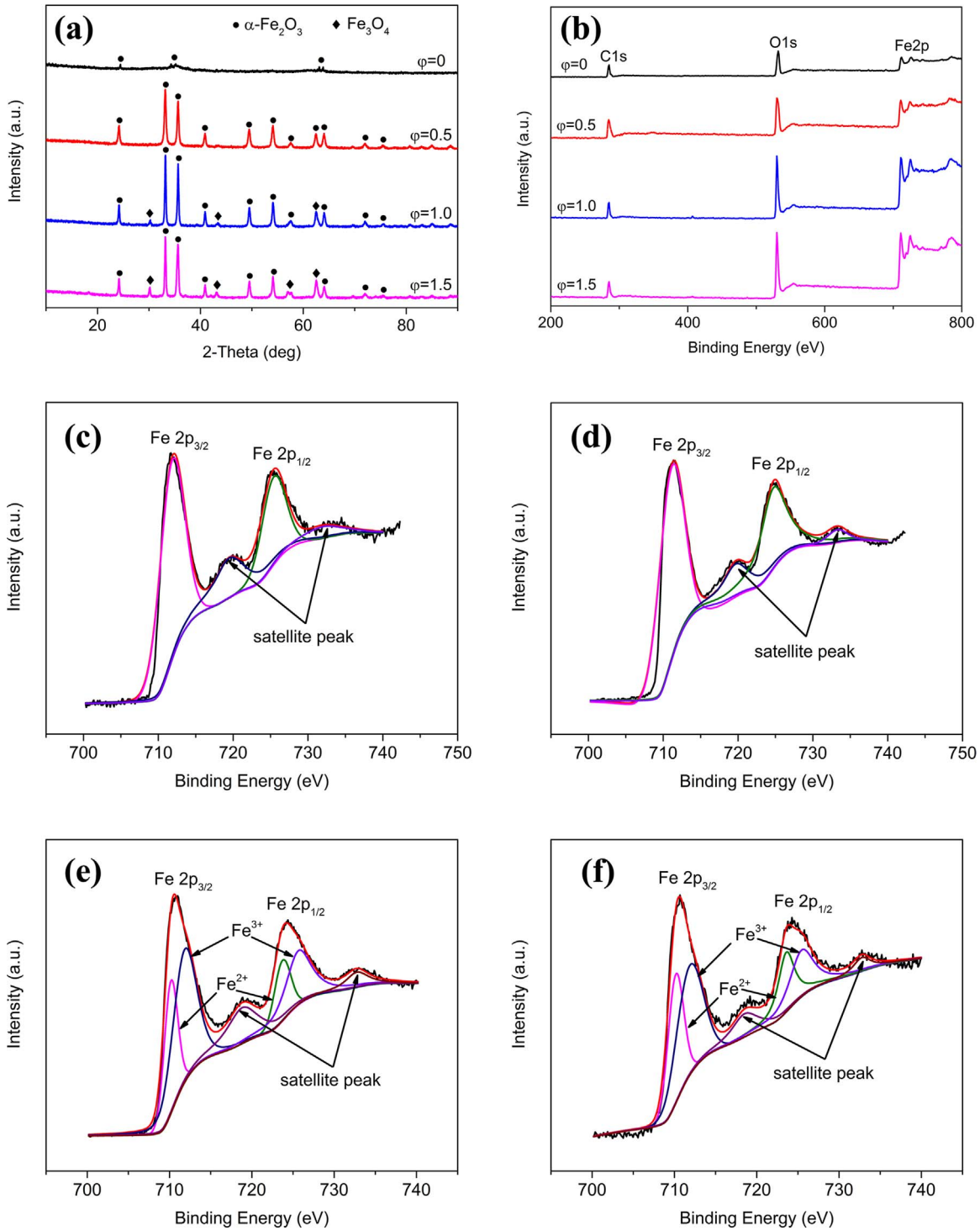

Fig. 6. (a) XRD patterns, (b) survey XPS spectra and (c–f) high resolution Fe2p XPS spectra of SCS products with different φ: (c) φ = 0; (d) φ = 0.5; (e) φ = 1.0; (f) φ = 1.5.

with different φ, they are investigated by FE-SEM, as shown in Fig. 3. It can be clearly observed in Fig. 3(a) that φ = 0 product exhibits a uniform appearance of urchin-like particles in the micrometer size range and the high magnification FE-SEM image shows that these microparticles are composed of abundant straight and radially grown nanoneedles with an average length of ~ 200 nm. The nanoneedle morphology may be due to the topotactic transformation between metal hydroxides and oxides, that the hydrolysis of Fe^{3+} triggered by OH^- with continuous energy input (pyrolysis reaction in Fig. 2(a)) contributes to the formation of hexagonal close-packed (*hcp*) α-FeOOH, which can improve the needle-like growth of α-Fe_2O_3 with wide bases and narrow tips, that is, the growth along a- and b-directions of *hcp* structure is inhibited but the aggregation along c-direction is allowed [29,30]. With the addition of fuel, the morphology of SCS products has totally changed. As seen from Fig. 3(b) and (c), both φ = 0.5 and 1.0 products present a cumuliform cloud-like cluster in micrometer size, which is assembled by a large number of irregular nanosheets with an average thickness of ~ 100 nm. By taking a closer look, a great many pores are apparently observed on the surface of these nanosheets due to the liberation of gases in the combustion process. The porous nanosheet morphology could be interpreted by three steps [31]: first, the aqueous solution condensed into flowing sol with the ability of film forming;

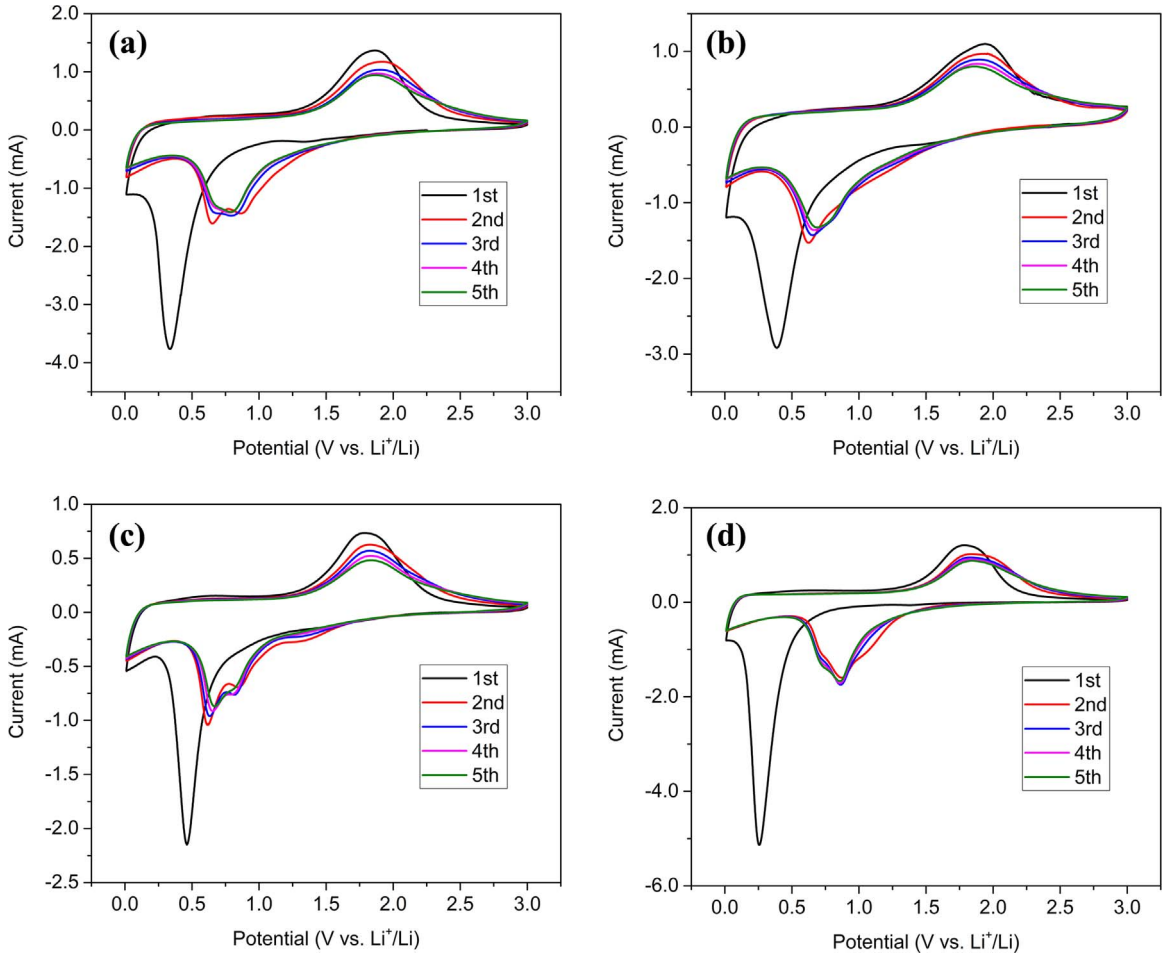

Fig. 7. CV curves of different φ anodes in the potential range of 0.01 and 3.0 V (vs. Li^+/Li) at a scan rate of 0.5 mV s^{-1}: (a) φ = 0; (b) φ = 0.5; (c) φ = 1.0; (d) φ = 1.5.

second, the sol evaporated into viscous gel with the formation of abundant pores; finally, the gel combusted with the release of gases, transforming the pore walls into porous sheets. With the increase of φ value, coral-like structure with some sporadic bulk particles can be observed in φ = 1.5 product, as shown in Fig. 3(d). Under higher magnification, it can be clearly seen that the coral-like structure is actually a porous framework, which consists of uniform nanoparticles with an average diameter of ~ 50 nm. These nanoparticles are believed to result from the stress-free and isotropic crystallization of face-centered cubic (*fcc*) Fe_3O_4 in combustion process [25].

To further clarify the morphology and microstructure of SCS products with different φ, TEM images are shown in Fig. 4. It can be clearly found in Fig. 4(a) that almost entire nanoneedles are assembled in a radial form from the center to the end of microparticle which looks like a sea urchin as a whole. The higher magnified image gives more details on the morphology of φ = 0 product that the nanoneedle has a large aspect ratio with the diameter of ~ 5 nm and the length of ~ 200 nm, which is in good agreement with the FE-SEM analysis in Fig. 3(a). With the addition of fuel, it is obvious in Fig. 4(b) and (c) that both φ = 0.5 and 1.0 products exhibit a porous sheet-like structure that a large quantity of well-structured single pores within 10 nm and a small quantity of irregular-shaped through pores beyond 50 nm are evidently distributed throughout the nanosheets, which is in accordance with the porous nanosheet morphology in Fig. 3(b) and (c). When compared, the highly magnified images reveal that the subunit of porous nanosheets in φ = 0.5 product is more like a crowd of worms but it transforms to irregular polygon with non-constant size in the range of 50–100 nm in φ = 1.0 product. Furthermore, when the φ value increases to 1.5, Fig. 4(d) shows uniform and well-dispersed nanoparticles with an average diameter of ~ 50 nm, which is in consistent with the FE-SEM analysis in Fig. 3(d). In addition, closer inspection reveals that the nanoparticle shows a nearly hexagonal geometry.

Based on the above analysis, all the SCS products exhibit porous structure to some extent, which could be owing to the release of gases from combustion reaction. To evaluate the specific surface area and pore size distribution of SCS products with different φ, N_2 adsorption-desorption isotherms and Barrett-Joyner-Halenda (BJH) pore size distribution curves are characterized, as shown in Fig. 5. It can be clearly observed that all the products exhibit a type-IV isotherm, which is ascribed to a mesoporous structure with uniform pores, as reported previously [15,32,33]. When compared, it is obvious that the hysteresis loop of φ = 0 product belongs to type H1 and its pore size distribution is relatively wide, with maximum at 20 nm, as depicted in Fig. 5(a). In contrast, the N_2 adsorption-desorption isotherms for φ = 0.5 and 1.0 products both show an H3-type hysteresis loop at P/P_0 = 0.45–1, indicating the presence of narrow and slit pores. As described in the inset of Fig. 5(b) and (c), BJH curves reveal that the pore size distributions for these products both are placed at 3–5 nm. With the increase of φ value, the N_2 adsorption-desorption isotherm in Fig. 5(d) is somewhat different. The isotherm shows a typical H2-type hysteresis loop, manifesting the heterogeneous distribution of pore sizes. It is obvious that the BJH curve (inset of Fig. 5(d)) displays a narrow main peak at about 5 nm and two wide small peaks at around 7 nm and 12 nm, further demonstrating the wide range of pore size distribution. In addition, according to the N_2 adsorption-desorption isotherms, the specific surface area of φ = 0.5 and 1.0 products estimated from BET method is 54.26 and 56.12 $m^2 g^{-1}$, respectively, which are higher than that of φ = 0 (27.22 $m^2 g^{-1}$) and 1.5 products (17.47 $m^2 g^{-1}$).

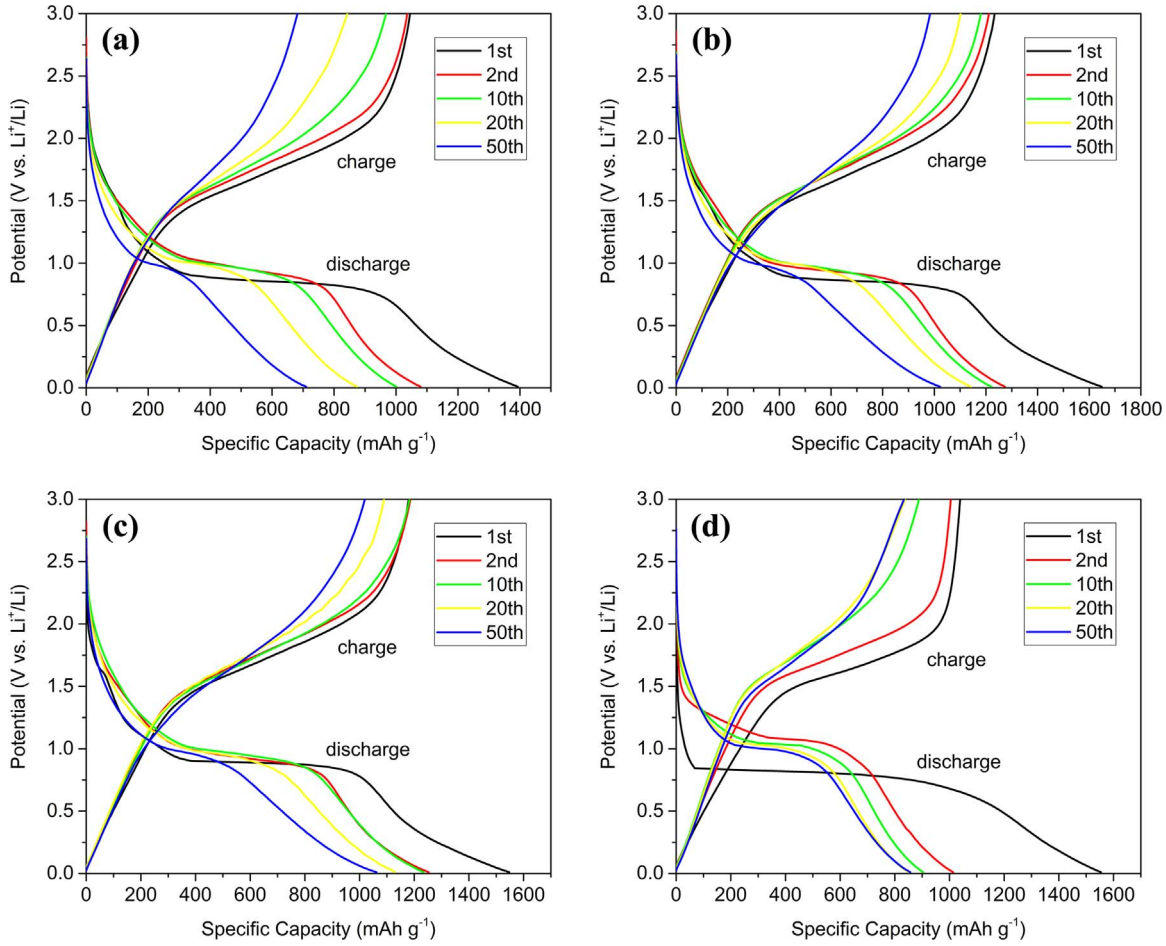

Fig. 8. Galvanostatic discharge and charge voltage profiles for 1st, 2nd, 10th, 20th and 50th cycles at the current density of 0.1 A g^{-1} of different φ anodes: (a) φ = 0; (b) φ = 0.5; (c) φ = 1.0; (d) φ = 1.5.

To clarify the crystal structure and phase composition of SCS products with different φ, XRD measurements were conducted, as presented in Fig. 6(a). It is clear that in the pattern of φ = 0 product, there are five tiny Bragg diffraction peaks centered at about 2θ = 24.1°, 35.6°, 39.2°, 62.4° and 63.9°, which correspond to the predominant reflection (012), (110), (006), (214) and (300) of α-Fe_2O_3 (JCPDS card No. 89-0599)[34]. The weak intensity of these peaks reveals the low crystallinity of α-Fe_2O_3 phase, namely, the major α-Fe_2O_3 phase in φ = 0 product is almost in amorphous form. According to the TG-DSC analysis in Fig. 1(a), the formation of amorphous α-Fe_2O_3 may be due to the low reaction temperature in endothermic process, which could not support the total and thorough crystallization of α-Fe_2O_3. When the φ value increases to 0.5, the crystalline α-Fe_2O_3 phase with sharp Bragg diffraction peaks have been detected and no additional peaks can be observed, demonstrating the pure crystalline α-Fe_2O_3 phase of φ = 0.5 product, which is in excellent agreement with the red color of product in Fig. 2(b). With the increase of φ value, it is obvious that both φ = 1.0 and 1.5 products exhibit a mixed crystalline phase of α-Fe_2O_3 (JCPDS card No. 89-0599) and Fe_3O_4 (JCPDS card No. 89-0691) according to their Bragg diffraction peak positions [35], which are well consistent with the black and red color of φ = 1.0 and 1.5 products in Fig. 2(c) and (d). Meanwhile, the intensity of Fe_3O_4 diffraction peaks in the pattern of φ = 1.5 product is slightly stronger than that of φ = 1.0 product, indicating the elevated proportion of Fe_3O_4 phase in φ = 1.5 product, which is in conformity to the decreased proportion of red part shown in Fig. 2(d).

To gain more insight into the phase composition of SCS products with different φ, XPS is used to analyze their chemical components, as presented in Fig. 6(b)–(f). On the one hand, the characteristic peaks of C1s, O1s and Fe2p are observed in wide scan XPS spectra (Fig. 6(b)) centered at about 285 (C1s), 530 (O1s), 711 (Fe $2p_{3/2}$) and 725 (Fe $2p_{1/2}$) eV, respectively, confirming the existence of these elementary components in all the products [36]. It is noteworthy that the characteristic peak of C1s appears inconspicuous when compared to the peaks of Fe2p and O1s, indicating the negligible amount of carbon in these products. With the increase of φ value, the intensities of Fe2p and O1s apparently enhance and their intensity ratio also rises, manifesting the elevated proportion of Fe^{2+} in FeO_x phase, which coincides with the above XRD analysis. On the other hand, the high resolution Fe2p XPS spectra of SCS products are shown in Fig. 6(c)–(f). It is evident in Fig. 6(c) and (d) that there are four peaks related to Fe $2p_{3/2}$, Fe $2p_{1/2}$ and their satellites, located at around 711.5, 725.2, 718.3 and 732.1 eV, respectively, which correspond to the electronic state of Fe^{3+} and point out the α-Fe_2O_3 phase in φ = 0 and 0.5 products [37], as evidenced by the above XRD analysis. By comparison, the high resolution deconvoluted Fe2p XPS spectra of φ = 1.0 and 1.5 products (Fig. 6(e) and (f)) exhibit four component peaks situated at about 709.2, 711.1, 722.4 and 724.5 eV, which are assigned to the Fe $2p_{3/2}$ binding energy (the former two) for Fe^{2+} and Fe^{3+}, and Fe $2p_{1/2}$ binding energy (the latter two) for Fe^{2+} and Fe^{3+} [23], respectively, suggesting the presence of two oxidation states of Fe in these products. Moreover, similar to the spectra of φ = 0 and 0.5 products, there are two charge transfer satellites of Fe $2p_{3/2}$ and Fe $2p_{1/2}$ positioned at 718 eV and 732 eV, respectively, which indicates the existence of α-Fe_2O_3 in φ = 1.0 and 1.5 products. Thus, it can be concluded that both φ = 1.0 and 1.5 products contain a mixed phase composition of α-Fe_2O_3 and Fe_3O_4, as confirmed by the

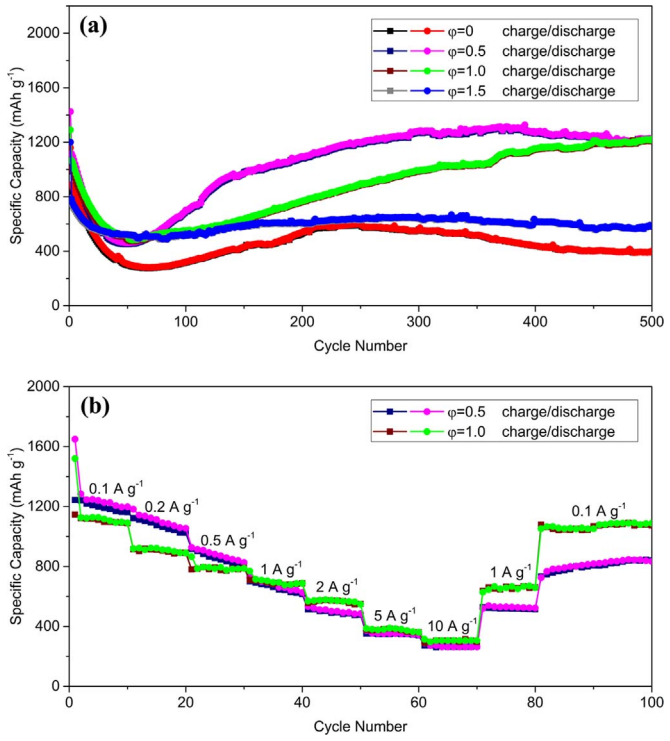

Fig. 9. (a) Cycling performance of different φ anodes at the current density of 1 A g^{-1} and (b) rate performance of φ = 0.5 and 1.0 anodes at various discharge and charge current densities from 0.1 A g^{-1} to 10 A g^{-1}.

Table 2
Comparison of reversible capacity with iron oxide anodes reported in open literatures.

Material	Reversible capacity (mA h g^{-1})	Current density (A g^{-1})	Ref.
α-Fe_2O_3/Fe_3O_4 porous nanosheets	1258 (500 cycles)	1	This work
3D hierarchical porous α-Fe_2O_3 nanosheets	1001 (1000 cycles)	1	[14]
Fe_2O_3@chitosan	732 (50 cycles)	0.1	[38]
α-Fe_2O_3/SWNT hybrid films	1100 (100 cycles)	0.1	[39]
porous α-Fe_2O_3 nanoparticles	841 (100 cycles)	0.5	[40]
porous graphene@C/Fe_3O_4 nanofibers	872 (100 cycles)	0.1	[44]
Fe/Fe_3O_4/C nanocomposites	755 (100 cycles)	0.1	[45]
Fe_3O_4/C nanosheets	647 (100 cycles)	0.2	[46]

above XRD analysis. In addition, it should be noted that the atomic ratio of Fe^{2+} to Fe^{3+} in φ = 1.0 and 1.5 products can be approximately quantified as the relative areas of two deconvoluted Fe $2p_{2/3}$ peaks in Fig. 6(e) and (f), which are calculated to be ~ 0.2 and ~ 0.3, respectively, indicating the elevated proportion of Fe_3O_4 phase in φ = 1.5 product, as proved by the XRD and survey XPS results in Fig. 6(a) and (b).

To evaluate the electrochemical performance of SCS products with different φ, CV curves of different φ anodes from the first to fifth cycle were characterized to understand the electrochemical reaction mechanism, as presented in Fig. 7. It is clear that all the CV curves of the first cycle are somewhat different from those of the subsequent cycles. In the first discharge process, a well-defined reduction peak is observed at about 0.5 V, which is attributed to reversible reduction of Fe^{3+} to Fe^0 and irreversible reaction involved in the decomposition of electrolyte to form a solid electrolyte interphase (SEI) film [38]. In turn, in the first charge process, the broad oxidation peak at around 1.7 V suggests the reversible oxidation of Fe° to Fe^{3+}, as depicted in Eq. (2) [39]. Noteworthily, the area of reduction peak is much larger than that of oxidation peak, further indicating the irreversible reaction in the first cycle. When compared the first cycle curves of different φ anodes, it is evident that the reduction peak in Fig. 7(c) and (d) is sharper than that in Fig. 7(a) and (b), at the same time, the reduction peak position in Fig. 7(c) is the most positive one. This could be ascribed to the various morphology and composition of different φ products, that is, the Fe_3O_4 phase in φ = 1.0 and 1.5 products could accelerate the stepwise reduction of Fe^{3+} to Fe^{2+} and Fe^{2+} to Fe^0, as described in Eqs. (3) and (4) [40], leading to a sharper shape of reduction peak, meanwhile, the nanosheet morphology of φ = 1.0 product causes parallel orientation of Li^+ diffusion pathway that increases the diffusion process efficiency [41]. Moreover, it can be clearly seen that since the second cycle, all the CV curves are nearly overlapped and both the reduction and oxidation peak positions are shifted to a more positive potential than those in the first cycle. As seen from Fig. 7(a), two reduction peaks at ~ 0.7 V and ~ 0.9 V are recorded in discharge process, which could be attributed to the insertion of Li^+ in crystalline and amorphous α-Fe_2O_3 to form *fcc* $Li_2Fe_2O_3$ and *hcp* $Li_xFe_2O_3$ phase, corresponding to the Eqs. (3) and (5) [14], respectively. By comparison, Fig. 7(b) shows that the φ = 0.5 anode undergoes a stepwise reductive reaction at ~ 0.7 V as depicted in Eqs. (3) and (4) due to its pure crystalline α-Fe_2O_3 phase. As for the φ = 1.0 anode, Fig. 7(c) shows two strong reduction peaks at ~ 0.6 V and ~ 0.8 V and a weak reduction peak at ~ 1.3 V, indicating the multi-step reductive reactions of Fe^{3+} and Fe^{2+} by Li^+ [39]. The reduction peak located at ~ 1.3 V is related to the insertion of Li^+ in crystalline α-Fe_2O_3 to form an intermediate *fcc* $Li_2Fe_2O_3$ phase (Eq. (3)), and then the $Li_2Fe_2O_3$ phase and Fe_3O_4 phase will further reduced to metallic Fe^0 with the formation of amorphous Li_2O (Eqs. (4) and (6)) at ~ 0.6 V and ~ 0.8 V, respectively [42]. With the increase of φ value, the amount of Fe_3O_4 phase in φ = 1.5 product elevates, resulting in the main reductive reaction of Fe_3O_4 phase at ~ 0.8 V (Eq. (6)), as shown in Fig. 7(d).

$$Fe_2O_3 + 6Li^+ + 6e^- \leftrightarrow 2Fe + 3Li_2O \quad (2)$$

$$Fe_2O_3 + 2Li^+ + 2e^- \rightarrow Li_2(Fe_2O_3) \quad (3)$$

$$Li_2(Fe_2O_3) + 4Li^+ + 4e^- \rightarrow 2Fe + 3Li_2O \quad (4)$$

$$Fe_2O_3 + xLi^+ + xe^- \leftrightarrow Li_xFe_2O_3 \quad (5)$$

$$Fe_3O_4 + 8Li^+ + 8e^- \leftrightarrow 3Fe + 4Li_2O \quad (6)$$

Fig. 8 shows the galvanostatic discharge and charge voltage profiles of different φ anodes in selected cycles at the current density of 0.1 A g^{-1}. It can be clearly observed that the initial specific discharge and charge capacities are 1393.2 and 1045.5 mA h g^{-1} for φ = 0 anode, 1648.7 and 1233.9 mA h g^{-1} for φ = 0.5 anode, 1547.6 and 1180.1 mA h g^{-1} for φ = 1.0 anode, 1554.2 and 1039.1 mA h g^{-1} for φ = 1.5 anode, which lead to an initial Coulombic efficiency of 75.1%, 74.8%, 76.3% and 66.9%, respectively. The capacity loss is mainly due to the irreversible reactions related to the decomposition of electrolyte and the formation of SEI film, which is well consistent with the area discrepancy between first reduction and oxidation peaks in the corresponding CV curves. It is worth noting that the φ = 0.5 anode owns the highest initial specific discharge capacity and the φ = 1.0 anode exhibits the least irreversible capacity loss. This phenomenon may be ascribed to the high theoretical capacity of crystalline α-Fe_2O_3 (ca. 1005 mA h g^{-1}) phase in φ = 0.5 product and the good electronic conductivity of Fe_3O_4 (ca. 2 × 10^4 S m^{-1}) phase in φ = 1.0 product [13,40]. In contrast to the φ = 1.0 anode, an impressive decrease in both initial specific capacity and Coulombic efficiency can be observed in Fig. 8(d), which may be owing to the small specific surface area and wide pore size distribution of φ = 1.5 product, as evidenced by BET analysis in Fig. 5(d). Furthermore, it should be emphasized that since the second cycle, the specific capacity of all the anodes decreases gradually due to the activation process of electrode material, whilst the

corresponding Columbic efficiency sharply increases to ~ 99% in the following several cycles, demonstrating the rapid stabilization of SEI film.

Fig. 9(a) compares the cyclic capacity retention of different φ anodes at 1 A g^{-1} for 500 cycles. As can be seen, the φ = 0.5 and 1.0 anodes exhibit a sharp decline in discharge capacity in the initial 50 cycles and then the capacity increases significantly to ~ 1200 mA h g^{-1} after 500 cycles, whereas for the φ = 0 and 1.5 anodes, a slight decrease of discharge capacity can be detected in the initial 50 cycles and then the capacity stabilizes at ~ 400 mA h g^{-1} and ~ 600 mA h g^{-1} in the subsequent cycles, respectively. It should be noticed that the impressively high discharge capacity and superior capacity recovery in φ = 0.5 and 1.0 anodes could be ascribed to the porous nanosheet morphology and high specific surface area, that is, the porous nanosheets can not only shorten the transport length of Li^+ but also supply favorable accessibility for electrons, meanwhile, the high specific surface area can provide an appropriate electrode/electrolyte interface to facilitate fast charge transfer and minimize polarization effects [43]. In order to evaluate the stability of these two anodes, the rate capability of φ = 0.5 and 1.0 anodes is compared at varying current densities ranging from 0.1 A g^{-1} to 10 A g^{-1}. As shown in Fig. 9(b), the average specific discharge capacity for φ = 1.0 anode decreases from 1126.3 to 921.6, 786.2, 694.8, 574.5, 388.9 and 305.6 mA h g^{-1} when the current density increases from 0.1 to 0.2, 0.5, 1, 2, 5, 10 A g^{-1}, respectively. After the high-rate discharge and charge cycling, the current density is suddenly reduced to 0.1 A g^{-1}, with the average specific discharge capacity as high as 1090.6 mA h g^{-1} recovered, demonstrating its good stability, swift response and excellent reversibility, which is much better than that of the φ = 0.5 anode (the capacity recovery is only ~ 60% as the current density returned back from 10 to 0.1 A g^{-1}). The good rate capability of φ = 1.0 anode could be attributed to the appropriate proportion of Fe_3O_4 phase in φ = 1.0 product, namely, the Fe_3O_4 phase enhances the electronic conductivity of product, leading to the rapid transformation of Li^+ and electrons. According to the results presented above, the φ = 1.0 product exhibits the best electrochemical properties among all the SCS products, further suggesting that the morphological and compositional differences have a great influence on their electrochemical performance. In addition, Table 2 shows the electrochemical performance of φ = 1.0 anode in this study compared to the iron oxide anodes reported in open literatures [14,38–40,44–46]. It is obvious that the φ = 1.0 anode in our work has a higher reversible capacity and a more stable cycling performance than the reported other iron oxide anodes. The excellent electrochemical performance should be attributed to its distinct morphology and phase composition, that is, the porous nanosheets can not only shorten the transport length of Li^+ but also supply favorable accessibility for electrons, meanwhile, the appropriate proportion of Fe_3O_4 phase will enhance the electronic conductivity of product, leading to the rapid transformation of Li^+ and electrons.

4. Conclusions

In conclusion, nanostructured iron oxides with controllable morphology and composition were successfully prepared via one-pot SCS method just by tuning the molar ratio (φ) of fuel (glycine) to oxidizer (ferric nitrate). With the increase of φ value, the morphology evolved from uniform nanoneedles to porous nanosheets, and finally into aggregated nanoparticles, meanwhile, the phase composition changed from amorphous α-Fe_2O_3 to crystalline α-Fe_2O_3, and eventually into α-Fe_2O_3/Fe_3O_4 composites. When applied as anode materials, the as-prepared α-Fe_2O_3/Fe_3O_4 porous nanosheets (φ = 1.0 product) exhibited the best electrochemical properties compared with the other products, demonstrating a high reversible capacity of ~ 1200 mA h g^{-1} at the current density of 1 A g^{-1} and an excellent rate capacity. These superior electrochemical performances should be attributed to the distinct morphology and phase composition that the porous nanosheets can not only shorten the transport length of Li^+ but also supply favorable accessibility for electrons, meanwhile, the appropriate proportion of Fe_3O_4 phase will enhance the electronic conductivity of product, leading to the rapid transformation of Li^+ and electrons.

Acknowledgements

This work was financially supported by the National Natural Science Foundation Program of China (51574031, 51574030 and 51574029), the Natural Science Foundation Program of Beijing (2162027), the National 863 Program (2013AA031101), the China Postdoctoral Science Foundation (2016M591073) and the Fundamental Research Funds for the Central Universities (FRF-TP-15-062A1).

References

[1] M. Su, C. He, K. Shih, Facile synthesis of morphology and size-controlled α-Fe_2O_3 and Fe_3O_4 nano-and microstructures by hydrothermal/solvothermal process: the roles of reaction medium and urea dose, Ceram. Int. 42 (2016) 14793–14804.
[2] S. Gyergyek, D. Makovec, M. Jagodič, M. Drofenik, K. Schenk, O. Jordan, J. Kovač, G. Dražič, H. Hofmann, Hydrothermal growth of iron oxide NPs with a uniform size distribution for magnetically induced hyperthermia: structural, colloidal and magnetic properties, J. Alloy. Compd. 694 (2017) 261–271.
[3] J. Liu, Z. Wu, Q. Tian, W. Wu, X. Xiao, Shape-controlled iron oxide nanocrystals: synthesis, magnetic properties and energy conversion applications, CrystEngComm 18 (2016) 6303–6326.
[4] R. Ianoş, A. Tăculescu, C. Păcurariu, I. Lazău, Solution combustion synthesis and characterization of magnetite, Fe_3O_4, nanopowders, J. Am. Ceram. Soc. 95 (2012) 2236–2240.
[5] W. Wu, C.Z. Jiang, V.A. Roy, Designed synthesis and surface engineering strategies of magnetic iron oxide nanoparticles for biomedical applications, Nanoscale 8 (2016) 19421–19474.
[6] D. Toulemon, Y. Liu, X. Cattoën, C. Leuvrey, S. Bégin-Colin, B.P. Pichon, Enhanced collective magnetic properties in 2D monolayers of iron oxide nanoparticles favored by local order and local 1D shape anisotropy, Langmuir 32 (2016) 1621–1628.
[7] R. Barik, K.T. Leung, M. Mohapatra, Solvent specific synthesis of nanocorpse flowery lithiated iron oxide as an energy storage and gas sensing material, New J. Chem. 40 (2016) 475–484.
[8] S. Shamaila, T. Bano, A.K.L. Sajjad, Efficient visible light magnetic modified iron oxide photocatalysts, Ceram. Int. (2017), http://dx.doi.org/10.1016/j.ceramint.2017.07.193.
[9] H. Quan, B. Cheng, Y. Xiao, S. Lei, One-pot synthesis of α-Fe_2O_3 nanoplates-reduced graphene oxide composites for supercapacitor application, Chem. Eng. J. 286 (2016) 165–173.
[10] H. Chen, X. Huang, L.J. Zhou, G.D. Li, M. Fan, X. Zou, Electrospinning synthesis of bimetallic nickel-iron oxide/carbon composite nanofibers for efficient water oxidation electrocatalysis, ChemCatChem 8 (2016) 992–1000.
[11] Z. Wang, C. Liu, Preparation and application of iron oxide/graphene based composites for electrochemical energy storage and energy conversion devices: current status and perspective, Nano Energy 11 (2015) 277–293.
[12] J. Tucek, K.C. Kemp, K.S. Kim, R. Zboril, Iron-oxide-supported nanocarbon in lithium-ion batteries, medical, catalytic, and environmental applications, ACS Nano 8 (2014) 7571–7612.
[13] P. Taberna, S. Mitra, P. Poizot, P. Simon, J. Tarascon, High rate capabilities Fe_3O_4-based Cu nano-architectured electrodes for lithium-ion battery applications, Nat. Mater. 5 (2006) 567–573.
[14] K. Cao, L. Jiao, H. Liu, Y. Liu, Y. Wang, Z. Guo, H. Yuan, 3D hierarchical porous α-Fe_2O_3 nanosheets for high-performance lithium-ion batteries, Adv. Energy Mater. 5 (2015) 4646–4652.
[15] P. Yang, J. Xie, C. Guo, C.M. Li, Soft-to network hard-material for constructing both ion-and electron-conductive hierarchical porous structure to significantly boost energy density of a supercapacitor, J. Colloid Interface Sci. 485 (2017) 137–143.
[16] A.M. Bruck, C.A. Cama, C.N. Gannett, A.C. Marschilok, E.S. Takeuchi, K.J. Takeuchi, Nanocrystalline iron oxide based electroactive materials in lithium ion batteries: the critical role of crystallite size, morphology, and electrode heterostructure on battery relevant electrochemistry, Inorg. Chem. Front. 3 (2016) 26–40.
[17] J. Livage, M. Henry, J.P. Jolivet, C. Sanchez, Chemical synthesis of fine powders, MRS Bull. 15 (1990) 18–25.
[18] M.A. Raza, Z. Kanwal, A. Rauf, A.N. Sabri, S. Riaz, S. Naseem, Size-and shape-dependent antibacterial studies of silver nanoparticles synthesized by wet chemical routes, Nanomaterials 6 (2016) 74.
[19] J. Zhou, X. Liu, W. Cai, Y. Zhu, J. Liang, K. Zhang, Y. Lan, Z. Jiang, G. Wang, Y. Qian, Wet-chemical synthesis of hollow red-phosphorus nanospheres with porous shells as anodes for high-performance lithium-ion and sodium-ion batteries, Adv. Mater. (2017), http://dx.doi.org/10.1002/adma.201700214.
[20] A. Ali, H. Zafar, M. Zia, I. Haq, A.R. Phull, J.S. Ali, A. Hussain, Synthesis, characterization, applications, and challenges of iron oxide nanoparticles, Nanotechnol. Sci. Appl. 9 (2016) 49–67.
[21] F. Li, J. Ran, M. Jaroniec, S.Z. Qiao, Solution combustion synthesis of metal oxide nanomaterials for energy storage and conversion, Nanoscale 7 (2015)

17590–17610.
[22] A. Thomas, C. Janáky, G.F. Samu, M.N. Huda, P. Sarker, J.P. Liu, V. Van Nguyen, E.H. Wang, K.A. Schug, K. Rajeshwar, Time-and energy-efficient solution combustion synthesis of binary metal tungstate nanoparticles with enhanced photocatalytic activity, ChemSusChem 8 (2015) 1652–1663.
[23] X. Wang, M. Qin, F. Fang, B. Jia, H. Wu, X. Qu, A.A. Volinsky, Effect of glycine on one-step solution combustion synthesis of magnetite nanoparticles, J. Alloy. Compd. 719 (2017) 288–295.
[24] M. Huang, M. Qin, P. Chen, B. Jia, Z. Chen, R. Li, Z. Liu, X. Qu, Facile preparation of network-like porous hematite (α-Fe_2O_3) nanosheets via a novel combustion-based route, Ceram. Int. 42 (2016) 10380–10388.
[25] A. Varma, A.S. Mukasyan, A.S. Rogachev, K.V. Manukyan, Solution combustion synthesis of nanoscale materials, Chem. Rev. 116 (2016) 14493–14586.
[26] W. Wen, J. Wu, Nanomaterials via solution combustion synthesis: a step nearer to controllability, RSC Adv. 4 (2014) 58090–58100.
[27] J. Zhao, Y. Shao, J. Zha, H. Wang, Y. Yang, S. Ruan, G. Yang, J. Chen, Large-scale preparation of crinkly NiO layers as anode materials for lithium-ion batteries, Ceram. Int. 42 (2016) 3479–3484.
[28] Z. Cao, M. Qin, B. Jia, Y. Gu, P. Chen, A.A. Volinsky, X. Qu, One pot solution combustion synthesis of highly mesoporous hematite for photocatalysis, Ceram. Int. 41 (2015) 2806–2812.
[29] X. Mou, X. Wei, Y. Li, W. Shen, Tuning crystal-phase and shape of Fe_2O_3 nanoparticles for catalytic applications, CrystEngComm 14 (2012) 5107–5120.
[30] W. Yu, L. Hui, Preparation of nano-needle hematite particles in solution, Mater. Res. Bull. 34 (1999) 1227–1231.
[31] J. Deng, L. Kang, G. Bai, Y. Li, P. Li, X. Liu, Y. Yang, F. Gao, W. Liang, Solution combustion synthesis of cobalt oxides (Co_3O_4 and Co_3O_4/CoO) nanoparticles as supercapacitor electrode materials, Electrochim. Acta 132 (2014) 127–135.
[32] M. Kim, J. Jeong, W.I. Cho, W. Kim, Synthesis of graphitic ordered mesoporous carbon with cubic symmetry and its application in lithium-sulfur batteries, Nanotechnology 27 (2016) 125401.
[33] S. Chen, Z. Chen, Y. Luo, M. Xia, C. Cao, Silicon hollow sphere anode with enhanced cycling stability by a template-free method, Nanotechnology 28 (2017) 165404.
[34] L. Zajíčková, P. Synek, O. Jašek, M. Eliáš, B. David, J. Buršík, N. Pizúrová, R. Hanzlíková, L. Lazar, Synthesis of carbon nanotubes and iron oxide nanoparticles in MW plasma torch with $Fe(CO)_5$ in gas feed, Appl. Surf. Sci. 255 (2009) 5421–5424.
[35] J. Han, X. Zong, Z. Wang, C. Li, A hematite photoanode with gradient structure shows an unprecedentedly low onset potential for photoelectrochemical water oxidation, Phys. Chem. Chem. Phys. 16 (2014) 23544–23548.
[36] Z. Geng, Y. Lin, X. Yu, Q. Shen, L. Ma, Z. Li, N. Pan, X. Wang, Highly efficient dye adsorption and removal: a functional hybrid of reduced graphene oxide-Fe_3O_4 nanoparticles as an easily regenerative adsorbent, J. Mater. Chem. 22 (2012) 3527–3535.
[37] T. Yamashita, P. Hayes, Analysis of XPS spectra of Fe^{2+} and Fe^{3+} ions in oxide materials, Appl. Surf. Sci. 254 (2008) 2441–2449.
[38] T.A. Nguyen, I.T. Kim, S.W. Lee, Chitosan-tethered iron oxide composites as an antisintering porous structure for high-performance Li-ion battery anodes, J. Am. Ceram. Soc. 99 (2016) 2720–2728.
[39] Z. Cao, B. Wei, α-Fe_2O_3/single-walled carbon nanotube hybrid films as high-performance anodes for rechargeable lithium-ion batteries, J. Power Sources 241 (2013) 330–340.
[40] D. Maiti, V. Aravindan, S. Madhavi, P.S. Devi, Electrochemical performance of hematite nanoparticles derived from spherical maghemite and elongated goethite particles, J. Power Sources 276 (2015) 291–298.
[41] H. Heli, H. Yadegari, A. Jabbari, Low-temperature synthesis of LiV_3O_8 nanosheets as an anode material with high power density for aqueous lithium-ion batteries, Mater. Chem. Phys. 126 (2011) 476–479.
[42] J. Guo, Y. Yang, W. Yu, X. Dong, J. Wang, G. Liu, T. Wang, Synthesis of α-Fe_2O_3, Fe_3O_4 and Fe_2N magnetic hollow nanofibers as anode materials for Li-ion batteries, RSC Adv. 6 (2016) 111447–111456.
[43] Z. Xing, Z. Ju, Y. Zhao, J. Wan, Y. Zhu, Y. Qiang, Y. Qian, One-pot hydrothermal synthesis of nitrogen-doped graphene as high-performance anode materials for lithium ion batteries, Sci. Rep.-UK 6 (2016) 26146.
[44] J. He, S. Zhao, Y. Lian, M. Zhou, L. Wang, B. Ding, S. Cui, Graphene-doped carbon/Fe_3O_4 porous nanofibers with hierarchical band construction as high-performance anodes for lithium-ion batteries, Electrochim. Acta 229 (2017) 306–315.
[45] M. Zhang, M. Cao, Y. Fu, L. Xing, Q. Wang, X. Xue, Ultrafast/stable lithium-storage electrochemical performance of Fe/Fe_3O_4/carbon nanocomposites as lithium-ion battery anode, Mater. Lett. 185 (2016) 282–285.
[46] Q. Xin, L. Gai, Y. Wang, W. Ma, H. Jiang, Y. Tian, Hierarchically structured Fe_3O_4/C nanosheets for effective lithium-ion storage, J. Alloy. Compd. 691 (2017) 592–599.